Inorg. Chem. **2006**, *45*, 10058–10065

Structural and Magnetic Studies on Cyano-Bridged Rectangular Fe_2M_2 (M = Cu, Ni) Clusters

Wei Liu, Cai-Feng Wang, Yi-Zhi Li, Jing-Lin Zuo,* and Xiao-Zeng You

Coordination Chemistry Institute and the State Key Laboratory of Coordination Chemistry, School of Chemistry and Chemical Engineering, Nanjing University, Nanjing 210093, P. R. China

Received July 20, 2006

Using the tricyano precursor, $(Bu_4N)[(Tp)Fe(CN)_3]$ (Tp = Tris(pyrazolyl) hydroborate) (**1**), four new tetranuclear clusters, $[(Tp)Fe(CN)_3Cu(Tp)]_2 \cdot 2H_2O$ (**2**), $[(Tp)Fe(CN)_3Cu(bpca)]_2 \cdot 4H_2O$ (**3**) (bpca = bis(2-pyridylcarbonyl)amidate anion), $[(Tp)Fe(CN)_3Ni(tren)]_2(ClO_4)_2 \cdot 2H_2O$ (**4**) (tren = tris(2-amino)ethylamine), and $[(Tp)Fe(CN)_3Ni(bipy)_2]_2[(Tp)Fe(CN)_3]_2 \cdot 6H_2O$ (**5**) (bipy = 2,2′-bipyridine), have been synthesized and structurally characterized. The four clusters possess similar square structures, where Fe^{III} and M^{II} (M = Cu^{II} or Ni^{II}) ions alternate at the rectangle corners. There exist intermolecular π–π stacking interactions through pyrazolyl groups of Tp^- ligands in complexes **2** and **4**, which lead to 1D chain structures. Complex **5** shows a 3D network structure through the coexistence of π–π stacking effects and hydrogen-bonding interactions. Magnetic studies show intramolecular ferromagnetic interactions in all four clusters. The exchange parameters are +11.91 and +1.38 cm^{-1} for clusters **2** and **3**, respectively, while uniaxial molecular anisotropy can be detected in complex **3** due to the distorted core in its molecular structure. Complex **4** has a ground state of $S = 3$ and shows SMM behavior with an effective energy barrier of $U = 18.9$ cm^{-1}. Unusual spin-glass-like dynamic relaxations are observed for complex **5**.

Introduction

Single-molecule magnetism has received considerable attention in the past decade since its first discovery in the oxo-manganese family.[1] With the combination of a high-spin ground state and negative uniaxial anisotropy, single-molecule magnets (SMMs) exhibit a significant energy barrier to spin reorientation.[2] This bistability makes them potentially applicable in high-density data storage and quantum computing.[3] Either designing clusters with more spin carriers or choosing proper bridging ligands to mediate ferromagnetic interaction between paramagnetic centers is required to achieve a high-spin ground state.[4] A mature and efficient method has not yet been discovered for the creation of molecule anisotropy: although some transition metal atoms have large anisotropy themselves, it is not easy to retain that at the whole-molecule level owing to their unpredictable arrangement in the cluster and other factors.[2,5–6] On the other hand, single-molecule magnetism is single-cluster behavior. However, in the synthetic process, the clusters may be connected, ferromagnetically or antiferromagnetically, by such intermolecular interactions as $\pi-\pi$ stacking and hydrogen-bonding interactions.[7] These interactions have important effects on the molecular magnetic properties, sometimes even diminishing or destroying the SMM behavior.

* To whom correspondence should be addressed. E-mail: zuojl@nju.edu.cn. Fax: +86-25-83314502.

(1) (a) Sessoli, R.; Tsai, H.-L.; Schake, A. R.; Wang, S.; Vincent, J. B.; Folting, K.; Gatteschi, D.; Christou, G.; Hendrickson, D. N. *J. Am. Chem. Soc.* **1993**, *115*, 1804−1816. (b) Sessoli, R.; Gatteschi, D.; Caneschi, A.; Novak, M. A. *Nature (London)* **1993**, *365*, 141−143.
(2) Gatteschi, D.; Sessoli, R. *Angew. Chem., Int. Ed.* **2003**, *42*, 268−297.
(3) (a) Christou, G.; Gatteschi, D.; Hendrickson, D. N.; Sessoli, R. *MRS Bull.* **2000**, *25*, 66−71 and references therein. (b) Garanin, D. A.; Chudnovsky, E. M. *Phys. Rev. B* **1997**, *56*, 11102−11118.
(4) (a) Tasiopoulos, A. J.; Vinslava, A.; Wernsdorfer. A.; Abboud, K. A.; Christou, G. *Angew. Chem., Int. Ed.* **2004**, *43*, 2117−2121. (b) Murugesu, M.; Habrych, M.; Wernsdorfer, W.; Abboud, K. A.; Christou, G. *J. Am. Chem. Soc.* **2004**, *126*, 4766−4767. (c) Aromi, G.; Parsons, S.; Wernsdorfer, W.; Brechin, E. K.; McInnes, E. J. L. *Chem. Commun.* **2005**, 5038−5040. (d) Moragues-Cánovas, M.; Helliwell, M.; Ricard, L.; Rivière, E.; Wernsdorfer, W.; Brechin, E.; Mallah, T. *Eur. J. Inorg. Chem.* **2004**, 2219−2222.
(5) (a) Collison, D.; Murrie, M.; Oganesyan, V. S.; Piligkos, S.; Poolton, N. R. J.; Rajaraman, G.; Smith, G. M.; Thomson, A. G.; Timko, G. A.; Wernsdorfer, W.; Winpenny, R. E. P.; McInnes, E. J. L. *Inorg. Chem.* **2003**, *42*, 5293−5303. (b) Barra, A. L.; Gatteschi, D.; Sessoli, R. *Chem.—Eur. J.* **2000**, *6*, 1608−1614.
(6) Beltran, L. M. C.; Long, J. R. *Acc. Chem. Res.* **2005**, *38*, 325−334.
(7) (a) Lecren, L.; Wernsdorfer, W.; Li, Y.-G.; Roubeau, O.; Miyasaka, H.; Clérac, R. *J. Am. Chem. Soc.* **2005**, *127*, 11311−11317. (b) Ge, C.-H.; Cui, A.-L.; Ni, Z.-H.; Jiang, Y.-B.; Zhang, L.-F.; Ribas, J.; Kou, H.-Z. *Inorg. Chem.* **2006**, *45*, 4883−4885.

10.1021/ic061347r CCC: $33.50
Published on Web 11/11/2006

Cyanide is a classical bridging ligand in the research for magnetic materials due to its convenience for designing the structure and conformation of the molecules and its efficiency for tuning the magnetic interaction.[8] High-nuclearity complexes are difficult to obtain with hexa- or octacyanometalates as building blocks since extended networks are favored for kinetic reasons in most cases, although a few examples of SMMs have been recently reported.[9] A rational approach to solve this problem is the introduction of multidentate blocking ligands.[6] The replacement of half the coordination sphere of the metal center inhibits the growth of an extended solid and may promote the construction of multinuclear clusters instead of polymers. Many cyano-containing building blocks have been designed, and several heterobimetallic SMMs have been prepared based on these.[10,11] Among the various structures, a few reports have been devoted to the structural and magnetic studies of heterobimetallic tetranuclear square clusters,[12,13] but only two display the slow relaxation of magnetization.[14] Using the precursor $(Bu_4N)[(Tp)Fe(CN)_3]$ (**1**) (Tp = hydrotris(pyrazolyl)borate), we have produced some clusters with various structures and interesting magnetic properties, including a face-centered cubic cluster $[(Tp)_8(H_2O)_6Cu_6Fe_8(CN)_{24}]^{4+}$ exhibiting SMM behavior[11a] and a pentanuclear SMM, $[(Tp)_2(Me_3tacn)_3Cu_3Fe_2(CN)_6](ClO_4)_4\cdot 2H_2O$.[11e] In this paper, four partially blocked salts, $[(Tp)Cu(H_2O)_2](ClO_4)$, $[(bpca)Cu(H_2O)_2](ClO_4)$, $Ni(tren)(ClO_4)_2$, and $Ni(bipy)_2(ClO_4)_2$, were chosen to react with **1**, affording four new molecular squares: $[(Tp)Fe(CN)_3Cu(Tp)]_2\cdot 2H_2O$ (**2**), $[(Tp)Fe(CN)_3Cu(bpca)]_2\cdot 4H_2O$ (**3**), $[(Tp)Fe(CN)_3Ni(tren)]_2(ClO_4)_2\cdot 2H_2O$ (**4**), and $[(Tp)Fe(CN)_3Ni(bipy)_2]_2[(Tp)Fe(CN)_3]_2\cdot 6H_2O$ (**5**). Herein, we report the syntheses and magnetic studies on these clusters; the factors that may affect SMM properties are also investigated.

Experimental Section

Materials and Physical Measurements. All chemicals were reagent-grade and used as received. $(Bu_4N)[(Tp)Fe(CN)_3]$[15a] and Hbpca[15b] were prepared by modified literature methods. Elemental analyses for C, H, and N were performed on a Perkin-Elmer 240C analyzer. Infrared spectra were recorded on a Vector22 Bruker spectrophotometer with KBr pellets in the 400−4000 cm^{-1} region. The magnetic susceptibility measurements on polycrystalline samples of complexes **2**−**5** were measured in the temperature range 1.8−300 K with a Quantum Design MPMS-XL7 SQUID magnetometer under an applied field ranging from 100 to 2000 Oe. Field dependences of magnetization were measured using a flux magnetometer in an applied field up to 70 kOe (50 kOe for complex **2**) generated by a conventional pulsed technique.

Caution! While no problems were encountered in this work, cyanides are toxic and perchlorate salts are potentially explosive. Thus, these starting materials should be handled with great care!

$[(Tp)Fe(CN)_3Cu(Tp)]_2\cdot 2H_2O$ (2). A solution of $[(Tp)Cu(H_2O)_2](ClO_4)$ (16.5 mg, 0.040 mmol) in 10 mL of ethanol was added to a solution of $(Bu_4N)[(Tp)Fe(CN)_3]$ (23.6 mg, 0.040 mmol) in 10 mL of ethanol, followed by the addition of 5 mL of water. Red-brown needlelike crystals of **2** were obtained after a week upon the evaporation of the solvent. Yield: 76%. Anal. Calcd (%) for $C_{42}H_{44}B_4Cu_2Fe_2N_{30}O_2$: C, 39.32; H, 3.46; N, 32.75. Found: C, 39.28; H, 3.43; N, 32.80. IR (KBr, cm^{-1}): 2127 (ν_{-CN}), 2176 ($\nu_{\mu-CN}$)

$[(Tp)Fe(CN)_3Cu(bpca)]_2\cdot 4H_2O$ (3). A green solution of $[(bpca)Cu(H_2O)_2](ClO_4)$ (17.0 mg, 0.040 mmol) in 10 mL of acetonitrile was added to a solution of $(Bu_4N)[(Tp)Fe(CN)_3]$ (23.6 mg, 0.040 mmol) in 15 mL of acetonitrile. Solids precipitated immediately. After the filtration, the solids were dissolved in minimum amounts of DMF, and orange rhombic single crystals were obtained in 2 days. Yield: 53%. Anal. Calcd (%) for $C_{48}H_{44}B_2Cu_2Fe_2N_{24}O_8$: C, 42.85; H, 3.30; N, 24.99. Found: C, 42.81; H, 3.25; N, 25.03. IR (KBr, cm^{-1}): 2145 (ν_{-CN}), 2168 ($\nu_{\mu-CN}$)

$[(Tp)Fe(CN)_3Ni(tren)]_2(ClO_4)_2\cdot 2H_2O$ (4). A solution of $Ni(tren)(ClO_4)_2$ (16.2 mg, 0.040 mmol) in 15 mL of methanol was added to a solution of $(Bu_4N)[(Tp)Fe(CN)_3]$ (23.6 mg, 0.040 mmol) in 15 mL of methanol. Red-brown needlelike crystals were obtained after a week upon the evaporation of the solvent. Yield: 81%. Anal. Calcd (%) for $C_{36}H_{60}B_2Cl_2Fe_2N_{26}Ni_2O_{10}$: C, 32.30; H, 4.52; N, 27.20. Found: C, 32.36; H, 4.57; N, 27.16. IR (KBr, cm^{-1}): 2119 (ν_{-CN}), 2152 ($\nu_{\mu-CN}$).

$[(Tp)Fe(CN)_3Ni(bipy)_2]_2[(Tp)Fe(CN)_3]_2\cdot 6H_2O$ (5). A solution of $Ni(bipy)_2(ClO_4)_2$ (22.8 mg, 0.04 mmol) in 10 mL of water/methanol (v/v = 1:1) was added to a solution of $(Bu_4N)[(Tp)Fe(CN)_3]$ (23.6 mg, 0.040 mmol) in 5 mL of methanol. Slow evaporation of the solvent at room temperature yielded red crystals of **5**. Yield: 74%. Anal. Calcd (%) for $C_{88}H_{84}B_4Fe_4N_{44}Ni_2O_6$: C, 47.23; H, 3.78; N, 27.54. Found: C, 47.28; H, 3.74; N, 27.60. IR (KBr, cm^{-1}): 2127 (ν_{-CN}), 2171 ($\nu_{\mu-CN}$).

X-ray Crystallography. The crystal structures of complexes **2**−**5** were determined on a Siemens (Bruker) SMART CCD diffracto-

(8) (a) Miller, J. S. *MRS Bull*. **2000**, *25*, 60−64. (b) Marvaud, V.; Decroix, C.; Scuiller, A.; Guyard-Duhayon, C.; Vaissermann, J.; Gonnet, F.; Verdaguer, M. *Chem.*−*Eur. J.* **2003**, *9*, 1677−1691. (c) Wang, S.; Zuo, J.-L.; Gao, S.; Song, Y.; Zhou, H.-C.; Zhang, Y.-Z.; You, X.-Z. *J. Am. Chem. Soc*. **2004**, *126*, 8900−8901.

(9) (a) Berlinguette, C. P.; Vaughn, D.; Canãda-Vilalta, C.; Galán-Mascarós, J. R.; Dunbar, K. R. *Angew. Chem., Int. Ed*. **2003**, *42*, 1523−1526. (b) Choi, H. J.; Sokol, J. J.; Long, J. R. *Inorg. Chem.* **2004**, *43*, 1606−1608. (c) Herrera, J. M.; Marvaud, V.; Verdaguer, M.; Marrot, J.; Kalisz, M.; Mathonière, C. *Angew. Chem., Int. Ed.* **2004**, *43*, 5468−5471. (d) Song, Y.; Zhang, P.; Ren, X.-M.; Shen, X.-F.; Li, Y.-Z.; You X.-Z. *J. Am. Chem. Soc.* **2005**, *127*, 3708−3709.

(10) Lescouëzec, R. L.; Toma, L. M.; Vaissermann, J.; Verdaguer, M.; Delgado, F. S.; Ruiz-Pérez, C.; Lloret, F.; Julve, M. *Coord. Chem. Rev.* **2005**, *249*, 2691−2729 and references therein.

(11) (a) Wang, S.; Zuo, J.-L.; Zhou, H.-C.; Choi, H. J.; Ke, Y. X.; Long, J. R.; You, X.-Z. *Angew. Chem. Int. Ed*. **2004**, *43*, 5940−5943. (b) Schelter, E. J.; Prosvirin, A. V.; Reiff, W. M.; Dunbar, K. R. *Angew. Chem., Int. Ed.* **2004**, *43*, 4912−4915. (c) Sokol, J. J.; Hee, A. G.; Long, J. R. *J. Am. Chem.* Soc. **2002**, *124*, 7656−7657. (d) Schelter, E. J.; Prosvirin, A. V.; Dunbar, K. R. *J. Am. Chem. Soc.* **2004**, *126*, 15004−15005. (e) Wang, C.-F.; Zuo, J.-L.; Bartlett, B. M.; Song, Y.; Long, J. R.; You, X.-Z. *J. Am. Chem. Soc.* **2006**, *128*, 7162−7163. (f) Li, D. F.; Parkin, S.; Wang, G. B.; Yee, G. T.; Clérac, R.; Wernsdorfer, W.; Holmes, S. M. *J. Am. Chem. Soc.* **2006**, *128*, 4214−4251. (g) Li, D. F.; Clérac, R.; Parkin, S.; Wang, G. B.; Yee, G. T.; Holmes, S. M. *Inorg. Chem.* **2006**, *45*, 5251−5253.

(12) (a) Oshio, H.; Onodera, H.; Tamada, O.; Mizutani, H.; Hikichi, T.; Ito, T. *Chem.*−*Eur. J.* **2000**, *6*, 2523−2530. (b) Kou, H.-Z.; Gao, S.; Li, C. -H.; Liao, D.-Z.; Zhou, B.-C.; Wang, R.-J.; Li, Y.-D. *Inorg. Chem.* **2002**, *41*, 4756−4762. (c) Kim, J.; Han, S.; Cho, I.-K.; Choi, K. Y.; Heu, M.; Yoon, S.; Suh, B. J. *Polyhedron* **2004**, *23*, 1333−1339. (d) Jiang, L.; Feng, X.-L.; Lu, T.-B.; Gao, S. *Inorg. Chem.* **2006**, *45*, 5018−5026.

(13) (a) Oshio, H.; Tamada, O.; Onodera, H.; Ito, T.; Ikoma, T.; Tero-Kubota, S. *Inorg. Chem.* **1999**, *38*, 5686−5689. (b) Oshio, H.; Yamamoto, M.; Ito, T. *Inorg. Chem.* **2002**, *41*, 5817−5820. (c) Toma, L. M.; Lescouëzec, R.; Cangussu, D.; Llusar, R.; Mata, J.; Spey, S.; Thomas, J. A.; Lloret, F.; Julve, M. *Inorg. Chem. Commun.* **2005**, *8*, 382−385.

(14) Li, D. F.; Parkin, S.; Wang, G. B.; Yee, G. T.; Prosvirin, A. V.; Holmes, S. M. *Inorg. Chem.* **2005**, *44*, 4903−4905.

(15) (a) Lescouëzec, R.; Vaissermann, J.; Lloret, F.; Julve, M.; Verdaguer, M. *Inorg. Chem.* **2002**, *41*, 5943−5945. (b) Kamiyama, A.; Noguchi, T.; Ito, T. *Inorg. Chem.* **2002**, *41*, 507−512.

Table 1. Crystallographic Data for Complexes **2**−**5**

	2	**3**	**4**	**5**
empirical formula	$C_{42}H_{44}B_4Cu_2Fe_2N_{30}O_2$	$C_{48}H_{44}B_2Cu_2Fe_2N_{24}O_8$	$C_{36}H_{60}B_2Cl_2Fe_2N_{26}Ni_2O_{10}$	$C_{88}H_{84}B_4Fe_4N_{44}Ni_2O_6$
M_r	1283.09	1345.47	1338.74	2238.05
cryst syst	monoclinic	monoclinic	triclinic	monoclinic
space group	$P2_1/n$	$C2/c$	$P\bar{1}$	$P2_1/c$
a (Å)	13.0187(9)	14.449(3)	9.784(3)	13.394(4)
b (Å)	13.6915(9)	20.996(5)	10.908(4)	13.944(4)
c (Å)	16.7856(11)	21.485(5)	15.208(5)	29.662(8)
α (deg)	90	90	109.989(8)	90
β (deg)	108.0220(10)	100.115(4)	90.076(9)	97.863(5)
γ (deg)	90	90	93.338(7)	90
V (Å^3)	2845.2(3)	6417(3)	1522.3(9)	5488(2)
Z	2	4	1	2
ρ_c(g cm^{-1})	1.498	1.393	1.460	1.354
F(000)	1304	2736	690	2296
T (K)	293(2)	298(2)	293(2)	293(2)
μ (mm^{-1})	1.303	1.163	1.233	0.920
index range	$-10 \le h \le 16$	$-17 \le h \le 17$	$-12 \le h \le 12$	$-16 \le h \le 16$
	$-16 \le k \le 15$	$-25 \le k \le 23$	$-13 \le k \le 12$	$-17 \le k \le 17$
	$-20 \le l \le 20$	$-26 \le l \le 20$	$-11 \le l \le 18$	$-36 \le l \le 36$
data/restraints/params	5577/0/370	6273/0/411	5977/1/382	10790/0/700
GOF(F^2)	1.073	1.312	1.016	0.997
R1[a], wR2[b] ($I > 2\sigma(I)$)	0.0439, 0.0994	0.0611, 0.1398	0.0566, 0.1156	0.0422, 0.0727
R1[a], wR2[b] (all data)	0.0570, 0.1034	0.0794, 0.1445	0.0764, 0.1217	0.0736, 0.0773

[a] $R1 = \sum||F_c| - |F_o||/\sum F_o|$. [b] $R2 = [\sum w(F_o^2 - F_c^2)^2/\sum w(F_o^2)]^{1/2}$.

meter using monochromated Mo Kα radiation ($\lambda = 0.71073$ Å) at room temperature. Cell parameters were retrieved using SMART software and refined using SAINT[16] on all observed reflections. Data were collected using a narrow-frame method with scan widths of 0.30° in ω and an exposure time of 10 s/frame. The highly redundant data sets were reduced using SAINT[16] and corrected for Lorentz and polarization effects. Absorption corrections were applied using SADABS[17] supplied by Bruker. Structures were solved by direct methods using the program SHELXL-97.[18] The positions of the metal atoms and their first coordination spheres were located from direct-method E maps; other non-hydrogen atoms were found using alternating difference Fourier syntheses and least-squares refinement cycles and, during the final cycles, were refined anisotropically. Hydrogen atoms were placed in calculated positions and refined as riding atoms with a uniform value of U_{iso}. Information concerning crystallographic data collection and structure refinement is summarized in Table 1.

Results and Discussion

Crystal Structures. Complexes **2**−**5** have very similar squarelike structures, and we note that this core geometry has been obtained previously with other metals and different capping ligands.[12−14] In the square unit, Fe^{III} and M^{II} ions (Cu^{II} for complexes **2** and **3**, Ni^{II} for complexes **4** and **5**) are located at alternating corners of the rectangle; each $[(Tp)Fe(CN)_3]^-$ unit uses its two cyanides to connect M^{II} ions, leaving the third terminal cyanide group free. The bond lengths and angles in the $[(Tp)Fe(CN)_3]^-$ unit are in good agreement with those in other complexes.[11a,12c,15a,19] Selected bond distances and angles for complexes **2**−**5** are collected in Tables 2−5.

Table 2. Selected Bond Lengths [Å] and Angles [deg] for **2**[a]

Fe(1)−N(1)	1.964(3)	Cu(1)−N(11)	2.013(2)
Fe(1)−N(3)	1.971(3)	Cu(1)−N(13)	2.002(3)
Fe(1)−N(5)	1.949(2)	Cu(1)−N(8)	1.986(3)
Fe(1)−C(10)	1.919(3)	Cu(1)−N(15)	1.949(2)
Fe(1)−C(11)	1.902(3)	C(11)−N(7)	1.154(4)
Fe(1)−C(12)	1.921(3)	C(12)−N(8)	1.127(4)
Cu(1)−N(9)	2.164(3)	C(10)−N(15)#1	1.148(4)
N(9)−Cu(1)−N(8)	97.48(10)	N(15)−Cu(1)−N(9)	116.37(10)
N(11)−Cu(1)−N(8)	89.78(11)	N(13)−Cu(1)−N(11)	88.09(10)
N(13)−Cu(1)−N(8)	174.35(11)	N(15)−Cu(1)−N(11)	153.70(11)
N(15)−Cu(1)−N(8)	90.17(10)	N(15)−Cu(1)−N(13)	89.43(10)
N(11)−Cu(1)−N(9)	89.69(10)	C(12)−N(8)−Cu(1)	176.8(3)
N(13)−Cu(1)−N(9)	87.74(10)	C(10)#1−N(15)−Cu(1)	171.9(3)

[a] Symmetry transformation used to generate equivalent atoms: #1 $-x$, $-y + 1$, $-z$.

Table 3. Selected Bond Lengths [Å] and Angles [deg] for **3**[a]

Fe(1)−N(1)	1.948(3)	Cu(1)−N(9)#1	2.178(3)
Fe(1)−N(3)	1.971(3)	Cu(1)−N(10)	2.000(3)
Fe(1)−N(5)	1.984(3)	Cu(1)−N(11)	1.954(3)
Fe(1)−C(10)	1.914(3)	Cu(1)−N(12)	2.025(3)
Fe(1)−C(11)	1.921(5)	C(10)−N(9)	1.156(4)
Fe(1)−C(12)	1.897(4)	C(11)−N(7)	1.148(6)
Cu(1)−N(8)	1.948(4)	C(12)−N(8)	1.190(5)
N(9)#1−Cu(1)−N(8)	93.81(13)	N(12)−Cu(1)−N(9)#1	96.57(13)
N(10)−Cu(1)−N(8)	97.13(14)	N(11)−Cu(1)−N(10)	80.18(14)
N(11)−Cu(1)−N(8)	150.68(14)	N(12)−Cu(1)−N(10)	161.48(14)
N(12)−Cu(1)−N(8)	95.83(14)	N(12)−Cu(1)−N(11)	81.74(14)
N(10)−Cu(1)−N(9)#1	95.72(13)	C(10)−N(9)−Cu(1)#1	167.0(3)
N(11)−Cu(1)−N(9)#1	115.51(14)	C(12)−N(8)−Cu(1)	178.7(3)

[a] Symmetry transformation used to generate equivalent atoms: #1 $-x + 1/2$, $-y + 1/2$, $-z + 1$.

The crystal structures for $[(Tp)Fe(CN)_3Cu(Tp)]_2 \cdot 2H_2O$ (**2**) and $[(Tp)Fe(CN)_3Cu(bpca)]_2 \cdot 4H_2O$ (**3**) are depicted in Figure 1. Complex **2** crystallizes in the monoclinic $P2_1/n$ space group, while complex **3** crystallizes in the monoclinic $C2/c$ space group. In both clusters, Cu^{II} ions have a distorted square pyramidal coordination sphere, which is completed by three N atoms from auxiliary ligands and two cyanide

(16) *SAINT-Plus*, version 6.02; Bruker Analytical X-ray System: Madison, WI, 1999.
(17) Sheldrick, G. M. *SADABSs An empirical absorption correction program*; Bruker Analytical X-ray Systems: Madison, WI, 1996.
(18) Sheldrick, G. M. *SHELXTL-97*; Universität of Göttingen: Göttingen, Germany, 1997.
(19) Wang, S.; Zuo, J.-L.; Zhou, H.-C.; Song, Y.; Gao, S.; You, X.-Z. *Eur. J. Inorg. Chem.* **2004**, 3681−3687.

Table 4. Selected Bond Lengths [Å] and Angles [deg] for **4**[a]

Fe(1)−N(1)	1.959(3)	Ni(1)−N(10)	2.134(3)
Fe(1)−N(3)	1.960(4)	Ni(1)−N(11)	2.089(3)
Fe(1)−N(5)	1.947(3)	Ni(1)−N(12)	2.077(4)
Fe(1)−C(10)	1.913(4)	Ni(1)−N(13)	2.056(4)
Fe(1)−C(11)	1.933(4)	C(10)−N(7)	1.144(5)
Fe(1)−C(12)	1.871(4)	C(11)−N(8)	1.112(5)
Ni(1)−N(7)	2.067(4)	C(12)−N(9)	1.180(5)
Ni(1)#1−N(9)	2.117(4)		
N(9)#1−Ni(1)−N(7)	91.39(13)	N(11)−Ni(1)−N(10)	164.94(13)
N(10)−Ni(1)−N(7)	92.67(13)	N(12)−Ni(1)−N(10)	92.32(15)
N(11)−Ni(1)−N(7)	100.76(13)	N(13)−Ni(1)−N(10)	84.27(14)
N(12)−Ni(1)−N(7)	90.81(14)	N(12)−Ni(1)−N(11)	94.26(16)
N(13)−Ni(1)−N(7)	173.09(15)	N(13)−Ni(1)−N(11)	83.09(14)
N(10)−Ni(1)−N(9)#1	85.69(13)	N(13)−Ni(1)−N(12)	83.14(16)
N(11)−Ni(1)−N(9)#1	87.18(14)	C(10)−N(7)−Ni(1)	161.7(3)
N(12)−Ni(1)−N(9)#1	177.10(13)	C(12)−N(9)−Ni(1)#1	173.8(3)
N(13)−Ni(1)−N(9)#1	94.55(15)		

[a] Symmetry transformation used to generate equivalent atoms: #1 $-x+1, -y+1, -z+1$.

Table 5. Selected Bond Lengths [Å] and Angles [deg] for **5**[a]

Fe(1)−N(1)	1.9760(19)	Ni(1)−N(10)	2.097(2)
Fe(1)−N(3)	1.990(2)	Ni(1)−N(11)	2.057(2)
Fe(1)−N(5)	1.959(2)	Ni(1)−N(12)	2.024(2)
Fe(1)−C(10)	1.912(3)	Ni(1)−N(13)	2.083(2)
Fe(1)−C(11)	1.919(2)	C(10)−N(7)	1.144(3)
Fe(1)−C(12)	1.932(2)	C(11)−N(8)	1.139(2)
Ni(1)−N(7)	2.069(2)	C(12)−N(9)	1.144(2)
Ni(1)#1−N(9)	2.049(2)		
N(9)#1−Ni(1)−N(7)	92.98(8)	N(11)−Ni(1)−N(10)	78.56(8)
N(10)−Ni(1)−N(7)	172.58(8)	N(12)−Ni(1)−N(10)	95.20(8)
N(11)−Ni(1)−N(7)	94.52(8)	N(13)−Ni(1)−N(10)	89.45(7)
N(12)−Ni(1)−N(7)	91.41(8)	N(12)−Ni(1)−N(11)	171.58(8)
N(13)−Ni(1)−N(7)	88.54(8)	N(13)−Ni(1)−N(11)	95.54(8)
N(10)−Ni(1)−N(9)#1	89.83(8)	N(13)−Ni(1)−N(12)	78.61(8)
N(11)−Ni(1)−N(9)#1	90.78(8)	C(10)−N(7)−Ni(1)	171.71(16)
N(12)−Ni(1)−N(9)#1	94.89(8)	C(12)−N(9)−Ni(1)#1	169.81(16)
N(13)−Ni(1)−N(9)#1	173.37(8)		

[a] Symmetry transformation used to generate equivalent atoms: #1 $-x, -y, -z$.

nitrogen atoms. The Cu−N_{ligand} (ligand: Tp^- or bpca) distances are distributed in the range 2.002(3)−2.164(3) Å for **2** and 1.954(3)−2.025(3) Å for **3**, and the Cu−N_{cyano} distances are in the range 1.949(2)−1.986(3) Å for **2** and 1.948(4)−2.178(3) Å for **3**, all of which are in the normal range. The Cu−N≡C angles (171.9(3)−176.8(3)° for **2** and 167.0(3)−178.7(3)° for **3**) are somewhat deviated from strict linearity. The two edges of the rectangle are 5.001 and 5.028 Å in **2**, and 5.032 and 5.217 Å in **3**. Compared with complex **2**, the larger differences in both Cu−N≡C angles and edge lengths in **3** may introduce more structural distortions. The intramolecular Fe···Fe and Cu···Cu separations are 7.208 and 6.974 Å in **2**, and 7.228 and 7.269 Å in **3**, respectively. Due to the $\pi-\pi$ stacking effect between the pyrazole rings (N5, N6, C7, C8, C9) of the Tp^- ligand coordinated with Fe^{III} in **2**, there exist intermolecular interactions between adjacent clusters, which lead to the formation of 1D chains along the *a* direction (Figure S1). The closest pyrazole−pyrazole distance is 3.413 Å. The shortest intermolecular Cu···Cu, Fe···Cu, and Fe···Fe distances are 8.449, 8.456, and 7.832 Å, respectively. In complex **3**, there is no significant intermolecular interaction since the nearest pyridyl rings from adjacent molecules are not overlapped.

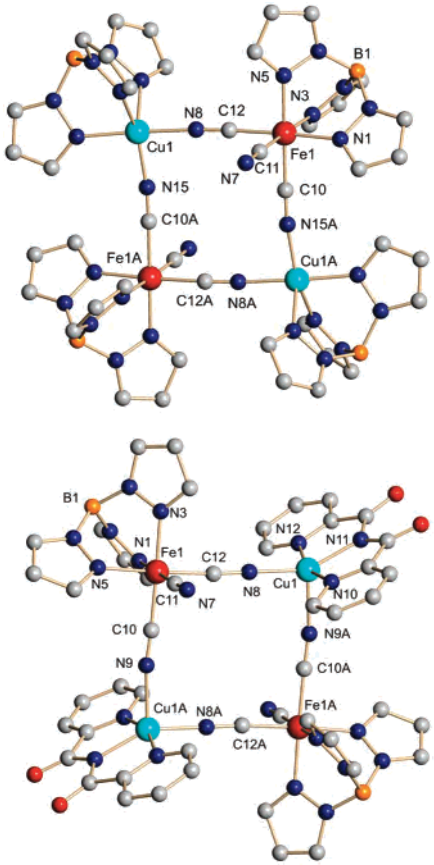

Figure 1. Core structure and labeling scheme of Fe_2Cu_2 clusters (**2**, upper; **3**, lower). Hydrogen atoms are omitted for clarity.

Complex **4** crystallizes in a lower-symmetry space group, triclinic $P\bar{1}$. The Ni^{II} ions are in a distorted octahedron coordination geometry constructed by four nitrogen atoms from the tren ligand and two nitrogen atoms from two cyanide bridges (Figure 2). The Ni−N_{tren} bond lengths range from 2.056(4) to 2.134(3) Å, and the Ni−N_{cyano} distances are from 2.067(4) to 2.117(4) Å. The large deviation of Ni−N≡C angles from linearity (161.7(3)−173.8(3)°) produces more distortion in square structure for cluster **4**. The intramolecular Fe···Ni separation is 5.042 and 5.156 Å, and the Fe···Fe and Ni···Ni separations are 7.434 and 6.982 Å. The pyrazolyl rings (N3, N4, C4, C5, and C6) from adjacent clusters are parallel to each other, and the shorter intermolecular pyrazolyl−pyrazolyl speration (3.697 Å) indicates the existence of $\pi-\pi$ stacking interactions, which results in the 1D chains along the 110 direction (Figure S2). The shortest intermolecular Fe···Fe, Fe···Ni, and Ni···Ni distances are 8.403, 6.426, and 8.945 Å, respectively.

Complex **5**, with monoclinic $P2_1/c$ space group, consists of a cationic rectangular unit, $[(Tp)Fe(CN)_3Ni(bipy)_2]_2^{2+}$, and two $[(Tp)Fe(CN)_3]^-$ anions. The nickel atom is six-coordinated, with the Ni−N distances in the range 2.024(2)−2.097(2) Å for Ni−N_{bipy} and 2.049(2)−2.069(2) Å for Ni−N_{cyano}. The Ni−N≡C angles (169.81(16)° and 171.71(16)°) are in the normal range. The intramolecular Fe···Ni distances are 5.090 and 5.100 Å, and the Fe···Fe and Ni···Ni separations are 7.473 and 6.927 Å, respectively. One-dimensional chains along the *b* direction are formed by

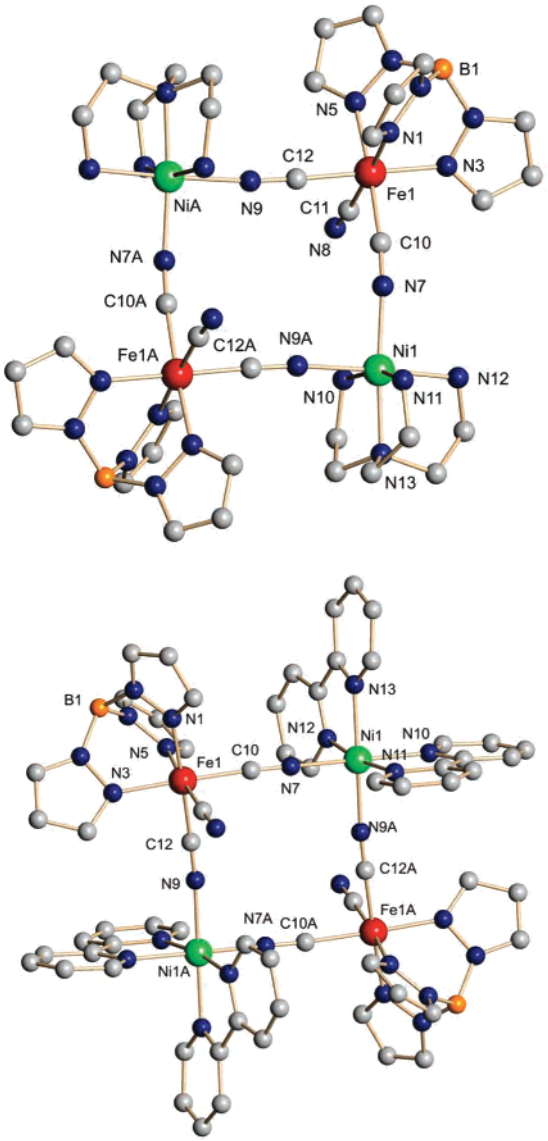

Figure 2. Core structure and labeling scheme of Fe_2Ni_2 clusters (**4**, upper; **5**, lower). Hydrogen atoms are omitted for clarity.

H-bonds (C20−H20···C4, 3.316 Å) and the $\pi-\pi$ stacking interactions through the pyridyl rings (N10, C18, C19, C20, C21, C22) which are separated by 3.651 Å (Figure 3). Neighboring chains are connected through hydrogen bonds occurring at C2−H2···N8 (3.470 Å). The separated $[(Tp)Fe(CN)_3]^-$ building blocks are arranged alternating in opposite directions and further connected to the above chains through H-bonds, thus leading to a 3D framework (Figure S3). The shortest intermolecular Ni···Ni, Fe1···Fe1, Fe1···Fe2, Fe···Ni1, and Fe···Ni2 distances are 9.231, 8.425, 8.309, 9.152, and 8.480 Å, respectively.

Magnetic Properties. Magnetic measurements were performed on polycrystalline samples of complexes **2**−**5**. The susceptibility variation with temperatures of **2** was measured in the temperature range 2.0−300 K (Figure 4). The $\chi_M T$ value is 2.28 emu K mol^{-1} at room temperature and increases moderately with decreasing temperature from 300 to 100 K, followed by a sharp increase to a maximum of 4.57 emu K mol^{-1} at 7.5 K, suggesting ferromagnetic coupling between Fe^{III} and Cu^{II} ions. The nearly saturated magnetization at 5 T (3.70 $N\beta$) confirms the $S = 2$ ground state (inset in Figure 4). On the basis of the structure, the Hamiltonian of **2** can be described as the following: $\hat{H} = -2J[\hat{S}_{Fe1}(\hat{S}_{Cu1} + \hat{S}_{Cu2}) + \hat{S}_{Fe2}(\hat{S}_{Cu1} + \hat{S}_{Cu2})]$, which includes only nearest-neighbor exchange. The best fit between 7.5 and 300 K gives $g = 2.39$, $J = +11.91$ cm^{-1}, indicating the existence of ferromagnetic interaction.

The magnetic properties of complex **3** are somewhat different from those of complex **2** (Figure 5). On decreasing temperature, $\chi_M T$ increases gradually from the room-temperature value of 1.60 emu K mol^{-1}, followed by a rapid increase below 45 K to a maximum of 2.04 emu K mol^{-1} at 5.0 K. The $\chi_M T$ data is simulated with the same Hamiltonian as **2**, and the fitting results between 8 and 300 K are $g = 2.05$ and $J = +1.38$ cm^{-1}. The magnetization value of 3.35 $N\beta$ in a 7 T magnetic field further confirms the nature of ferromagnetic interaction and the ground state of $S = 2$ (inset in Figure 5). In the M versus H/T plot, the nonsuperposition of the lines in different magnetic fields is observed (Figure 6), suggesting the existence of zero-field splitting. With the spin ground state $S = 2$, fits of the magnetization data using ANISOFIT[20] afford $D = -1.15$ cm^{-1}. However, the magnetic exchange constant for complex **3**, +1.38 cm^{-1}, is almost equivalent with the $|D|$ value. That is to say, the lowest lying excited spin state is about 2.76 cm^{-1} higher than the ground spin state, and the first excited spin state has considerable population;[21] for this reason the simulated D value from the temperature dependence of magnetization is inaccurate. Alternating current susceptibility studies carried out in the 1.8−10 K range in a 5Oe oscillating field at frequencies up to 1500 Hz for **3** show no evidence for magnetic ordering or slow paramagnetic relaxation.

The temperature dependence of susceptibility for complex **4** is displayed in Figure 7. Upon lowering the temperature, the $\chi_M T$ value increases continuously from the room-temperature value of 3.57 emu K mol^{-1}, reaching a maximum of 5.69 emu K mol^{-1} at 12 K, indicating ferromagnetic interaction between Fe^{III} and Ni^{II}. This can be further supported by the apparently unsaturated magnetization value of 4.97 $N\mu_B$ under a 7 T magnetic field (Figure S4). Below 12 K, $\chi_M T$ drops sharply, reaching 1.15 emu K mol^{-1} at 1.8 K, which could be attributed to the zero-field splitting[22] and/or weak antiferromagnetic interactions between the clusters. Using an approximate isotropic model similar to **2**, $\hat{H} = -2J[\hat{S}_{Fe1}(\hat{S}_{Ni1} + \hat{S}_{Ni2}) + \hat{S}_{Fe2}(\hat{S}_{Ni1} + \hat{S}_{Ni2})]$, the $\chi_M T$ value was fitted above 12 K including the intermolecular interaction, and the best result gives $g = 2.22$, $J = +4.52$ cm^{-1}, and $zJ' = -0.14$ cm^{-1}. The magnetization variation for **4** at different magnetic fields was recorded between 1.8 and 10 K (Figure 8), which shows a similar trend like the ever-reported trinuclear SMM $Mn^{III}_2M^{III}$ (M = Cr, Fe).[9b] The nonsuperposition of the isofield lines indicates the presence of significant zero-field splitting. Under the magnetic field of

(20) Shores, M. P.; Sokol, J. J.; Long, J. R. *J. Am. Chem. Soc.* **2002**, *124*, 2279−2292.
(21) Berseth, P. A.; Sokol, J. J.; Shores, M. P.; Heinrich, J. L.; Long, J. R. *J. Am. Chem. Soc.* **2000**, *122*, 9655−9662.
(22) Mydosh, J. A. *Spin glasses: An Experimental Introduction*; Taylor & Francis: London, 1993.

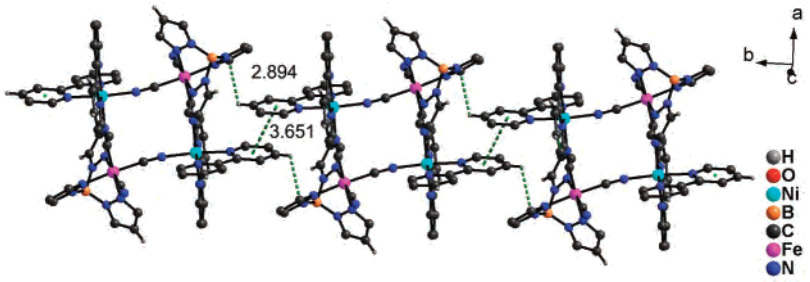

Figure 3. Pseudochain of complex **5** running along the *b* axis.

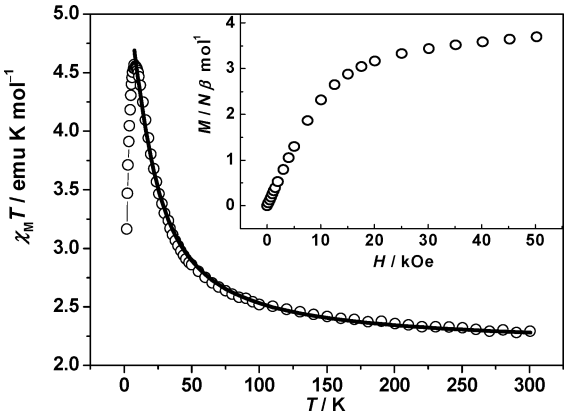

Figure 4. Temperature dependence of $\chi_M T$ in the dc field of 1000 Oe for complex **2**. The solid line corresponds to the best-fit curve. The inset shows the magnetization versus the applied magnetic field at 1.8 K.

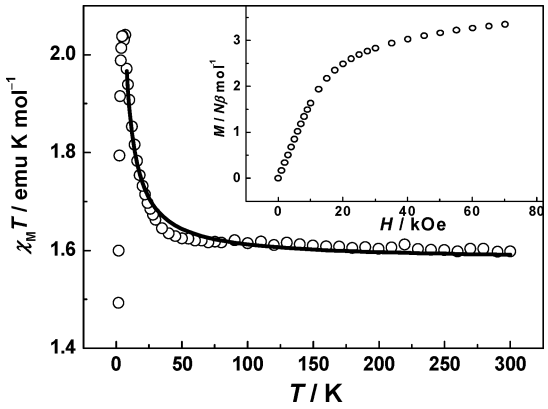

Figure 5. Temperature dependence of $\chi_M T$ in the dc field of 100 Oe for complex **3**. The solid line corresponds to the best-fit curve. The inset shows the magnetization versus the applied magnetic field at 1.8 K.

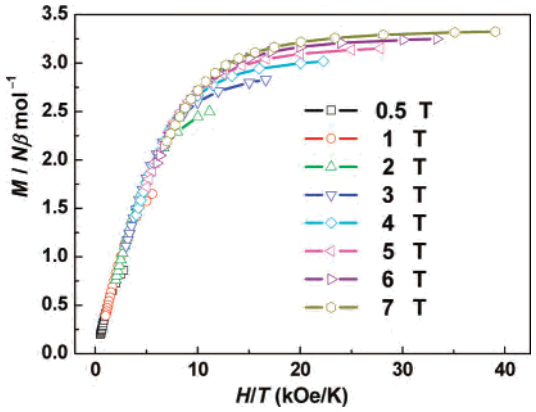

Figure 6. Plot of magnetization vs H/T for **3** between 1.8 and 10 K. The solid line is simply to guide the eye.

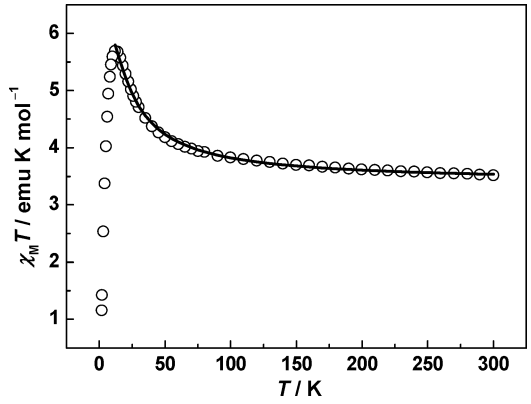

Figure 7. Temperature dependence of $\chi_M T$ in the DC field of 2000 Oe for complex **4**. The solid line corresponds to the best-fit curve.

5 kOe, the maximum of the magnetization corresponds to the existence of intermolecular interactions. However, for the same reason as for complex **3**, the simulated D value, -3.85 cm^{-1}, is suspect.

To investigate the dynamic nature of complex **4**, the ac susceptibility was measured in the frequency range 1−1488 Hz at 1.8−10 K (Figure 9). The obvious frequency-dependent signals in both in-phase ($\chi_{M'}T$) and out-of-phase susceptibilities ($\chi_{M''}$) can be observed below 5 K. The frequency dependence of the peak temperature shift (ΔT_p) of $\chi_{M'}$ leads to $\phi = (\Delta T_p/T_p)/\Delta(\log f) = 0.20$, which excludes the spin-glass property.[22] The relaxation rate can be calculated from the frequency dependence of the peak temperature (T_p) of $\chi_{M''}$ by the Arrhenius equation $\tau = \tau_0 \exp(\Delta E/k_B T)$, where τ, τ_0, ΔE, and k_B represent relaxation time, pre-exponential factor, relaxation energy barrier, and Boltzmann constant, respectively. Least-squares fitting gives $\tau_0 = 1.4 \times 10^{-8}$ s and an effective spin-reversal barrier of $U_{eff} = 18.9$ cm^{-1} (inset in Figure 9). $\chi_{M'}$ and $\chi_{M''}$ signals indicate the existence of slow magnetization relaxation and support that complex **4** behaves like an SMM, although there are intermolecular interactions.[7a,9b]

The temperature variation of susceptibility for complex **5** is displayed in Figure 10. The considerably larger $\chi_M T$ value at room temperature (6.81 emu K mol^{-1}; $C = 0.125 \sum g^2 S_i(S_i+1) = 3.50$ emu·K·mol^{-1}) may be ascribed to the orbital contributions from Fe^{III} and Ni^{II}, and the exchange interaction between Fe^{III} and Ni^{II} ions even at room temperature, because complex **5** is so easily magnetized that the magnetization value reaches as high as 1.80 $N\mu_B$ under a 100 Oe external magnetic field (inset in Figure 10). Upon lowing the

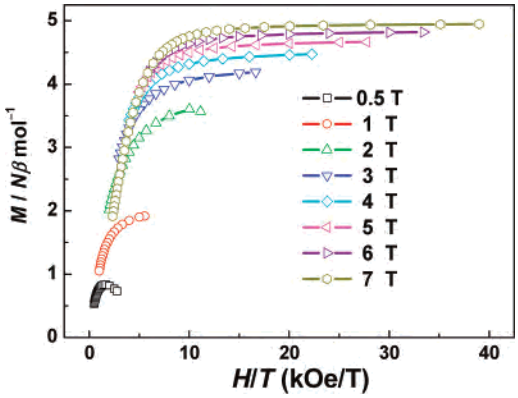

Figure 8. Plot of magnetization vs H/T for **4** between 1.8 and 10 K. The solid line is simply to guide the eye.

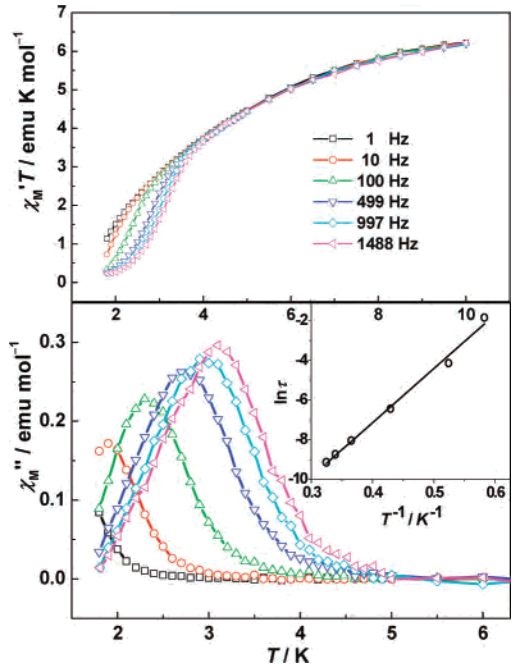

Figure 9. Frequency dependence of the in-phase $\chi_M'T$ product and out-of-phase$\chi_{M''}$ versus T for **4** in a 5 Oe field oscillating at frequencies between 1 and 1488 Hz. The inset is the Arrhenius fit for the lnτ vs T^{-1} plot.

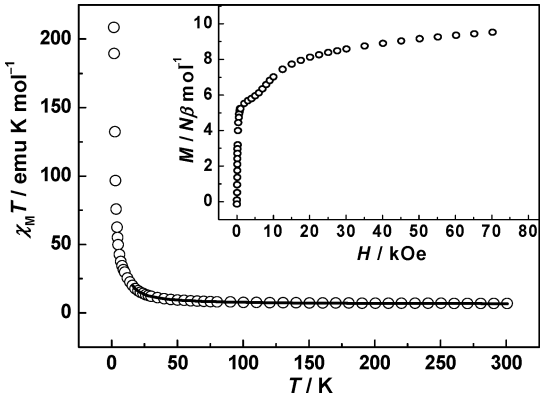

Figure 10. Temperature dependence of χ_MT in the dc field of 100 Oe for complex **5**. The solid line corresponds to the best-fit curve. The inset shows the magnetization versus the applied magnetic field at 1.8 K.

temperature, χ_MT increases smoothly, reaching 12.1 emu K mol^{-1} at 30 K, which is then followed by a continuous and sharp increase to 208.6 emu K mol^{-1} at 1.8 K, indicating

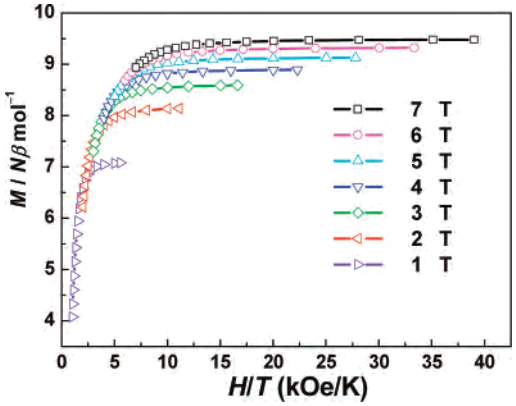

Figure 11. Plot of magnetization vs H/T for **5** between 1.8 and 10 K. The solid line is simply to guide the eye.

long-range ferromagnetic interaction resulting from strong intermolecular interactions.[23] The experimental χ_MT value is the summation of the tetranuclear square, with the same model as complex **4**, and two free paramagnetic anions. Considering the intermolecular interaction using the mean field theory approximation, the best fit between 18 and 300 K gives $g = 2.67$, $J = +7.36$ cm^{-1}, and $zJ' = +0.58$ cm^{-1}, indicating both intramolecular and intermolecular ferromagnetic interaction.

In the low magnetic field, the magnetization of **5** increases rapidly, reaching 5.22 $N\mu_B$ at 1000 Oe. Above the field of 17 kOe, the magnetization value increases more slowly, reaching 9.52 $N\mu_B$ at 7 T, which is consistent with the $S = 4$ ground state with respect to the large spin−orbit coupling. The temperature dependence of magnetization under different fields was collected between 1.8 and 10 K. As shown in Figure 11, the nonsuperposition of the isofield lines confirms the existence of significant zero-field splitting. Because of the paramagnetic component in the molecule, the data cannot be simulated without subtracting the paramagnetic contribution.

To investigate the dynamic nature, the ac susceptibility of complex **5** was measured in the frequency range 1−1488 Hz at 1.8−10 K (Figure 12). Both the in-phase ($\chi_{M'}$) and out-of-phase ($\chi_{M''}$) susceptibility signals display obvious frequency-dependence, which precludes the occurrence of 3D long-range ordering. The frequency dependence of the peak temperature shift (ΔT_p) of $\chi_{M'}$ is measured by a parameter $\phi = (\Delta T_p/T_p)/\Delta(\log f) = 0.08$, consistent with canonical spin-glass behavior.[22] If we simulate the relaxation rate using the Arrhenius equation $\tau = \tau_0 \exp(\Delta E/k_BT)$, least-squares fitting gives $\tau_0 = 8.8 \times 10^{-15}$ s and an effective spin-reversal barrier of $U_{eff} = 47.4$ cm^{-1}. The relaxation time is located beyond the normal range for typical SMMs (usually $>10^{-12}$ s). More studies should be done to fully understand the physical properties of **5**.

The ferromagnetic intramolecular interactions in the four square clusters are due to the orthogonal character of the t_{2g}

(23) (a) Lescouëzec, R.; Vaissermann, J.; Toma, L. M.; Carrasco, R.; Lloret, F.; Julve, M. *Inorg. Chem.* **2004**, *43*, 2234−2236. (b) Toma, L. M.; Lescouëzec, R.; Pasán, J.; Ruiz-Pérez, C.; Vaissermann, J.; Cano, J.; Carrasco, R.; Wernsdorfer, W.; Lloret, F.; Julve, M. *J. Am. Chem. Soc.* **2006**, *128*, 4842−4853.

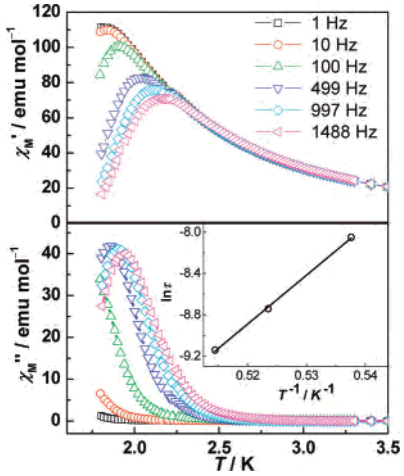

Figure 12. Frequency dependence of the in-phase $\chi_{M'}$ and out-of-phase $\chi_{M''}$ products versus T for **5** in a 5 Oe field oscillating at frequencies between 1 and 1488 Hz. The inset is the Arrhenius fit for the lnτ vs T^{-1} plot.

magnetic orbit for low-spin Fe^{III} ions and e_g magnetic orbit for M^{II} ions (M^{II} is Cu^{II} for **2** and **3**, and Ni^{II} for **4** and **5**). Compared with complex **2**, the structure differences in complex **3** may create much distortion in the cluster and generate the uniaxial anisotropy. For further investigation, Ni^{II} ions with larger single-ion spin−orbit coupling were introduced into the tetranuclear cluster system to replace Cu^{II} ions. Complex **4** possesses considerable uniaxial anisotropy; the frequency dependence of ac susceptibility and the relaxation rate in the normal range for SMMs confirm its SMM-like behavior. Molecular anisotropy was also observed in complex **5**, but the ac measurements indicate spin-glass-like behavior with long-range magnetic interaction.[24]

In summary, four tetranuclear square clusters, $[(Tp)Fe(CN)_3CuTp]_2\cdot 2H_2O$ (**2**), $[(Tp)Fe(CN)_3Cu(bpca)]_2\cdot 4H_2O$ (**3**), $[(Tp)Fe(CN)_3Ni(tren)]_2(ClO_4)_2\cdot 2H_2O$ (**4**), and $[(Tp)Fe(CN)_3Ni(bipy)_2]_2[(Tp)Fe(CN)_3]_2\cdot 6H_2O$ (**5**), were synthesized and structurally characterized. Magnetic studies show that the molecular anisotropy is greatly determined by the single-ion anisotropy and the distortion of the molecular structure. Importantly, intermolecular interactions affect the SMM-like behavior to some extent. Therefore, different magnetic properties, from ferromagnetism to SMM-like and spin-glass-like behaviors, are observed for these clusters with nearly the same geometry and topology. The foregoing results are useful for the design and synthesis of new SMMs in future.

Acknowledgment. This work was supported by the National Natural Science Foundation of China, the Major State Basic Research Development Program (Grant No. 2006CB806104), the Program for New Century Excellent Talents in University of China (NCET-04-0469), and Natural Science Foundation of Jiangsu Province (BK2006512). The authors are grateful to Professor Song Gao at Peking University for helpful discussions.

Supporting Information Available: Additional figures. X-ray crystallographic files in CIF format for **2**−**5**. This material is available free of charge via the Internet at http://pubs.acs.org.

IC061347R

(24) Gîrtu, M. A.; Wynn, C. M.; Fujita, W.; Awaga, K.; Epstein, A. J. *Phys. Rev. B* **1998**, *57*, 11058−11061.